

SCIENTIFIC REPORTS



OPEN

Understanding the Connection between Nanoparticle Uptake and Cancer Treatment Efficacy using Mathematical Modeling

Terisse A. Brocato¹, Eric N. Coker², Paul N. Durfee¹, Yu-Shen Lin³, Jason Townson³, Edward F. Wyckoff⁴, Vittorio Cristini^{5,6,7}, C. Jeffrey Brinker^{1,4,8,9,10} & Zhihui Wang^{5,6}

Nanoparticles have shown great promise in improving cancer treatment efficacy while reducing toxicity and treatment side effects. Predicting the treatment outcome for nanoparticle systems by measuring nanoparticle biodistribution has been challenging due to the commonly unmatched, heterogeneous distribution of nanoparticles relative to free drug distribution. We here present a proof-of-concept study that uses mathematical modeling together with experimentation to address this challenge. Individual mice with 4T1 breast cancer were treated with either nanoparticle-delivered or free doxorubicin, with results demonstrating improved cancer kill efficacy of doxorubicin loaded nanoparticles in comparison to free doxorubicin. We then developed a mathematical theory to render model predictions from measured nanoparticle biodistribution, as determined using graphite furnace atomic absorption. Model analysis finds that treatment efficacy increased exponentially with increased nanoparticle accumulation within the tumor, emphasizing the significance of developing new ways to optimize the delivery efficiency of nanoparticles to the tumor microenvironment.

Cancer represents the 2nd major cause of death in the United States, and one out of eight women is estimated to develop invasive breast cancer in her lifetime¹. Breast cancer tumors are heterogeneous, and the series of events which cause them to grow, shrink, or metastasize are complex, involving interactions with and influences from their microenvironment². It is known that the heterogeneity of the breast cancer tumor greatly complicates our understanding of the disease and the development of effective treatment². In fact, most tumors are heterogeneous both phenotypically and functionally³, resulting in variable traits among different tumors. Understanding an individual's response based on these differing traits is essential for predicting and improving patient-specific treatment response.

Due to drug toxicity and non-specificity, a spectrum of different particles have been developed for both particle-based drug delivery and for imaging of particle distribution, including superparamagnetic iron oxide nanoparticles⁴, lipid bilayer encapsulated nanoporous silicon or mesoporous silica particles for drug/cargo delivery⁵⁻⁷, and silica based nanoparticles⁸, to name a few. Here, we discuss the use of mesoporous silica nanoparticles (MSNPs), which possess the benefits of a high cargo capacity, due to their immense internal surface area

¹Department of Chemical and Biological Engineering and Center for Biomedical Engineering, University of New Mexico, Albuquerque, NM, 87131, USA. ²Advanced Materials Lab, Sandia National Laboratories, Albuquerque, NM, 87106, USA. ³Department of Internal Medicine, Division of Molecular Medicine, the University of New Mexico, Albuquerque, NM, 87131, USA. ⁴Center for Micro-Engineered Materials, the University of New Mexico, Albuquerque, NM, 87131, USA. ⁵Center for Precision Biomedicine, Brown Foundation Institute of Molecular Medicine, University of Texas Health Science Center (UTHealth) McGovern Medical School at Houston, Houston, TX, 77030, USA. ⁶Department of Imaging Physics, University of Texas MD Anderson Cancer Center, Houston, TX, 77230, USA. ⁷Department of Nanomedicine, Methodist Hospital Research Institute, Houston, TX, 77030, USA. ⁸Cancer Research and Treatment Center, the University of New Mexico Health Sciences Center, Albuquerque, NM, 87131, USA. ⁹Department of Molecular Genetics and Microbiology, the University of New Mexico Health Sciences Center, Albuquerque, NM, 87131, USA. ¹⁰Self-Assembled Materials Department, Sandia National Laboratories, Albuquerque, NM, 87185, USA. Correspondence and requests for materials should be addressed to C.J.B. (email: cjbrink@sandia.gov) or Z.W. (email: Zhihui.Wang@uth.tmc.edu)

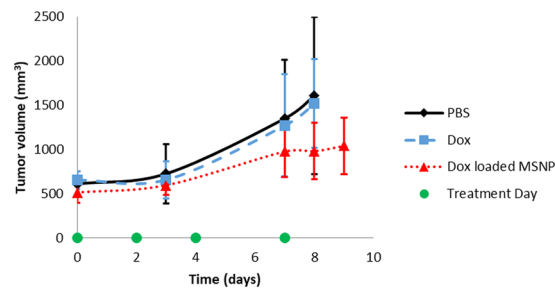


Figure 1. Average tumor volume measurements. Three treatment groups (7 mice/group, with standard deviation shown in error bars): PBS (control), free doxorubicin (Dox), and 50 nm MSNPs loaded with Dox. Each group's average tumor size is shown above. Measurements were taken on days 0, 3, 7, 8, and 9. Treatments were given on days 0, 2, 4, and 7. Individual mice data are shown in Supplementary Fig. S1.

(800–1000 m^2/g), facile surface modification to enable targeting, low toxicity, therapeutic effectiveness^{9,10}, and increased circulation time, therefore increasing total tumor drug uptake¹⁰. As a result, the effective therapeutic drug dosage is reduced when delivered using MSNPs relative to the free drug delivery case, minimizing treatment side effects.

Using an integrated mathematical modeling and experimental approach¹¹, our group has shown that nano-carrier mediated drug delivery of doxorubicin achieves equal cell kill efficacy at a dose only 20% of that of the corresponding free doxorubicin in a hepatocellular carcinoma cell model *in vitro*. In the present study, we use 50-nm diameter acetylated MSNPs, modified with polyethylene glycol (PEG) and polyethyleneimine (PEI) as first reported in Townson *et al.*¹². These acetylated MSNPs were found to be colloidal stable and non-toxic. They were shown to have reduced non-specific binding to cell types A549, A431, Hep3b and hepatocytes *in vitro*, as well as to endothelium and white blood cells, and were observed to remain in circulation over 6 hours post injection in a chorioallantoic membrane (chicken embryo) model¹². The increased circulation time of the acetylated MSNPs (>6 hrs) greatly improves their likelihood of entering the tumor and delivering effective drug dosages to cancer cells when compared to the circulation time of free drug (<2 hrs, $t_{1/2} = 1.68$ hrs)¹³.

A number of techniques have been developed to monitor the pharmacokinetics and biodistribution of nanoparticles in living animals, including optical fluorescent microscopy imaging^{14–16}, ultrasound¹⁷, *in vivo* bioluminescence (IVIS[®] using luciferase)^{18,19}, and PET, SPECT, and CT (as well as combinations of these techniques) using appropriate contrast agents^{14,15,20–22}. However, successful prediction of treatment outcome based solely on parameters measured from the biodistribution of nanoparticles is challenging because the distribution of nanoparticles and of drug are different and heterogeneous across tissues, organs, and even whole organisms. We have previously developed a mathematical model^{11,23} that predicts the fraction of tumor killed by chemotherapeutic treatment (denoted by f_{kill}) based on drug uptake and nanoparticle drug flux. f_{kill} was shown to be quadratic with respect to time, especially in the initial phase of a treatment. In the present study, we develop a mathematical theory based on this model^{11,23} in order to predict nanoparticle-based treatment efficacy using quantitative experimental data obtained from measured nanoparticle biodistribution.

Measurement of drug distribution *in vivo* is often difficult and expensive. Typically, quantitative analysis of nanoparticle biodistribution is done through organ dissection after injection of labeled nanoparticles, followed by imaging, using methods such as transmission electron microscopy or optical microscopy, or by elemental analysis using inductively coupled plasma-atomic emission²⁴. Nanoparticle distribution can also be measured *in vivo* using magnetic resonance imaging and magnetic particle imaging²⁴. Here, capitalizing on the low natural abundance of elemental silicon in mammals, we performed Si elemental analysis of the major organs in order to measure MSNP concentrations, and then compared these quantified MSNP accumulation values to changes in tumor volume. By using our theory to link measured tumor growth with nanoparticle distribution and concentration, and considering the effects of vasculature and diffusion characteristics, we were able to successfully predict the *in vivo* therapeutic efficacy of MSNP-delivered doxorubicin to 4T1 breast cancer tumors in mice.

Results and Discussion

Cancer stage at the time of diagnosis is demonstrated to be an important predictor of morbidity and survival²⁵. Five-year survival rates for breast cancer are 99% when diagnosed pre-metastasis, but with a significant reduction to only 25% five-year survival rate when the tumor has metastasized²⁵. In order to better understand the difficulties of effective therapeutic treatment when patients are diagnosed at a later stage, our experiments focused on treating tumors that were relatively large with distant metastases prior to the start of a treatment. Accordingly, we implemented a 4T1 cell line experiment in BALB/c mice, in order to study stage IV human breast cancer with metastasis in the presence of an active immune system.

Treatment efficacy between MSNPs loaded with doxorubicin (Dox) and free Dox was compared at the same dosage; phosphate buffered saline (PBS) was used as a control in a third treatment group. Tumor size measurements in mm^3 are shown in Fig. 1 for three groups of seven mice each treated using PBS (control), free Dox, or MSNPs loaded with Dox. Due to this treatment being administered at a later stage of breast cancer, it can be observed that free Dox treatment is not effective at a late stage; but the nanoparticle treatment shows some efficacy (see Supplementary Fig. S1 for each individual measurement). However, we note that statistically significant difference in tumor response between different treatment groups was not identified. This warrants additional

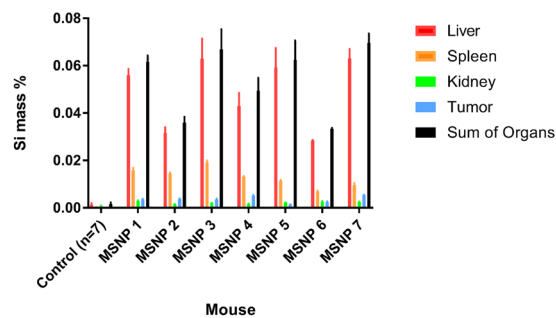


Figure 2. MSNP deposition (Si mass %) in liver, spleen, kidneys, tumor, sum of organs, and average Si concentration naturally in tissues (control group) taken post-sacrifice (day 9). Data were obtained using GFAA spectrophotometry. Error bars are calculated based on the standard additions method used to calculate standard deviation of Si concentrations.

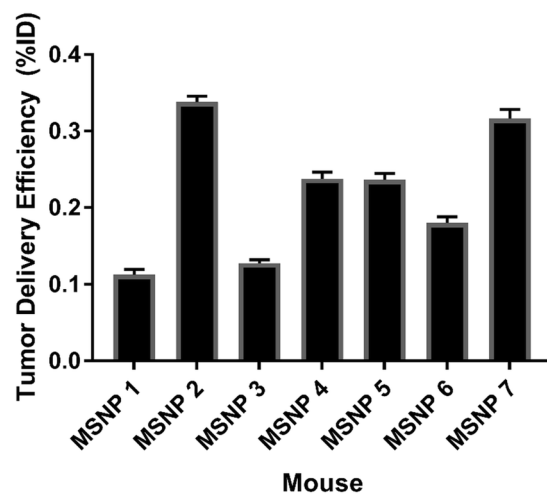


Figure 3. Tumor delivery efficiency (%ID). Data were obtained using GFAA spectroscopy. Naturally occurring Si (measured by testing control tumors in mice not exposed to MSNPs) was subtracted from absolute Si mass % in tumor. Standard deviation is shown in error bars ($n = 7$ for control and MSNP groups). Delivery efficiency calculation is described in Methods in section “Graphite Furnace Atomic Absorption Spectrophotometry.”

experiments on a larger scale with more data points to demonstrate the treatment efficacy for this particular nanoparticle.

In vivo biodistribution of nanoparticles based on size, shape, composition, and surface characteristics is still not well understood, as are the details of nanoparticle removal from circulation by the reticuloendothelial system²⁶. To gain a better understanding of these important parameters, we used graphite furnace atomic absorption (GFAA) to measure silicon (Si) concentration and distribution within tissues of interest²⁷. The Si concentration in the control (PBS) group was used as a baseline for the background Si concentration which occurs naturally in tissues (Si has important biofunctionality, and thus is found in trace quantities in many tissues). As expected, we observed that the amount of naturally occurring Si in the control tissues was low relative to the signal of MSNP in treated tissues (Fig. 2, control). Figure 2 shows measured values of elemental Si determined by GFAA, presented as the mass percentage of Si in the corresponding tissue being tested in mouse organs from the control and Dox loaded MSNP treatment groups after 9 days of treatment and sacrifice. The tissues tested were tumor, kidney, liver, spleen, as well as a measured sum of all organs. The sum of all organs tested corresponded to ~2–4.4% of the total injected Si dose, as shown in Supplementary Fig. S2.

Mice, even within the same treatment group, demonstrated a wide range of f_{kill} responses, indicated by the large standard deviation seen in tumor volumes in Fig. 1 (error bars). Moreover, the concentrations of Si deposited in the liver, spleen, kidney, and tumor were shown to vary without correlation between uptake in the tissues measured in our study (Fig. 2). For example, mice that had greater MSNP uptake in the liver did not have greater or lesser uptake in the tumor, see Fig. 3 for tumor delivery efficiency (%ID), and mice with less MSNP uptake in the tumor did not have less or more uptake in other organs. From our experiments here, we find that the MSNP delivery efficiency to the tumor is about 0.22%ID on average. Based on an extensive review of papers over the past ten years, Wilhelm *et al.* reports 0.7%ID as being the average tumor delivery efficacy using a multitude of particles, cancer types, and measurement methods, and mentions that, “it is possible that the amount of nanoparticles

Mouse	Si % in tumor	t_0 (time tumor begins to respond to treatment in days)	θ_f (quadratic response coefficient)	p -value	R^2 (quadratic)
MSNP 4	0.00513	—	0.4621	—	—
MSNP 7	0.00535	—	0.3068	—	—
MSNP 2	0.00372	0	0.0096	0.0030	0.9648
MSNP 3	0.00362	0	0.0067	0.0050	0.9499
MSNP 1	0.00360	0	0.0064	0.0110	0.9155
MSNP 5	0.00138	0	0.0027	0.1990	0.4728
MSNP 6	0.00260	0	0.0013	0.0060	0.9409

Table 1. Tumor f_{kill} coefficients (θ_f), as described by Eq. 4, show a similar order to Si deposition values. The Si deposition values are also shown in Fig. 2 (MSNP deposition) and in Fig. 4 (R^2 , θ_f , t_0), showing the exponential relation to the tumor f_{kill} coefficient calculated using Eq. 4. p -values and R^2 are calculated with respect to quadratic curves described in Eq. 4.

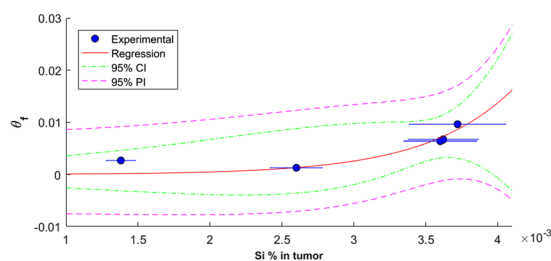


Figure 4. Si concentration and f_{kill} coefficient (θ_f) determination. θ_f , explained in Eq. 4, is predicted based on Si absolute mass percentage in tumor, as measured using graphite furnace atomic absorption (GFAA). $R^2 = 0.817$, $p_{.05} = 0.0007$ for quadratic f_{kill} coefficients calculated after 9 days of treatment and sacrifice. This was determined by the best fit between f_{kill} and Si concentration using an exponential fit (which represents the best fitting function among many we have tested, including linear and nonlinear functions, e.g., quadratic, sigmoidal, the Michaelis-Menton, and the Hill function). Experimental mouse tumor f_{kill} was determined using Eq. 2 for mice treated with MSNPs. Model mouse tumor f_{kill} was determined by optimizing values for t_0 (days in integer values), described in Eq. 4. Standard deviation for measured Si % in each mouse's tumor treated with MSNPs is shown for experimental values on the x-axis.

reaching cancer cells and their subcellular compartments *in vivo* is much less than 0.7%ID because nanoparticles need to cross the tumour extracellular matrix to reach the cancer cells²⁸. Hence, our data seems well consistent with Welhelm *et al.*'s paper. One paper used elemental analysis, ICP-AES, to measure silica nanoparticle concentration, of which the %ID was determined to be 0.29, 1.6, and 10.8%ID²⁹, most of the quantifications used to calculate the average of 0.7%ID in a tumor used PET scans as a method of quantification^{16,21,30,31}. Thus, the biodistribution of nanoparticles was observed to show significant variability, even amongst similar mice under the same treatment protocol. Blood volume fraction (i.e., the volume of the tumor occupied by blood vessels) was previously shown to be an important factor in predicting f_{kill} in human colorectal cancer metastasized to the liver³².

Many current nanoparticles have achieved the capability to release drugs at a nearly constant, sustained rate for a period of days, weeks, or even months^{33–35}, although this rate may be dependent on other physicochemical properties of the particles, such as the surface chemistry and pore size³⁶. *In vivo*, this nearly constant drug release rate results in an approximately unchanged rate of change of drug flux (denoted by F) across blood vessels. By further assuming a linear drug uptake by cancer cells, we have developed a special form of f_{kill} for predicting treatment efficacy for nanoparticle-based drug delivery systems²³. We found that tumor response *in vivo* to Dox loaded nanoparticles occurs quadratically over time, at least for the first several days ($f_{kill} = \theta_f \cdot t^2$, i.e., Eq. 4, where θ_f is the tumor f_{kill} coefficient; also see Methods), and have further validated this model using experiments on a breast cancer mouse model. Accordingly, we used this quadratic tumor response model to link the MSNP deposition with measured changes in tumor volume (relative to control). The quadratic tumor response coefficient (i.e., f_{kill} coefficient: θ_f) was determined to have an exponential relationship with MSNP deposition in the tumor tissue (Fig. 4); note that we simply applied a phenomenological approach to identification of the relationship between θ_f and Si deposition. θ_f was found to be predictable based on tumor silicon content with 95% confidence ($R^2 = 0.817$, $p_{.05} = 0.0007$) based on the quadratic curve for f_{kill} described in Eq. 4. This indicates that increasing chemotherapy drug delivery, using a MSNP transport vector, results in an exponentially greater rate of tumor kill. Values for comparison are shown in Table 1, along with statistics that indicate that most model values are statistically significant at 95% confidence except for MSNP 5. MSNP 4 and 7 did not show measurable response to treatment until day 7, resulting in only two data points; therefore, p -values for θ_f could not be determined due to an insufficient number of points. As such, these two mice were removed from further analysis. Together, this indicates that MSNP uptake is an important factor in determining tumor treatment efficacy. However, more tumor measurements and/or a longer experiment would be beneficial to validate statistical significance with the model predictions.

We then performed correlation analysis to compare model results (computed as $f_{\text{kill}} = 0.000172 \cdot e^{1664.39 \cdot Si} \cdot t^2$, where Si is tumor Si mass %) and the corresponding time course MSNP experimental data as shown in Fig. 1; also see Fig. S3. We obtained correlation coefficient $r=0.89$ and $p < 0.001$, and thus consider the model to be acceptable in predicting MSNP-based treatment outcome with absolute Si mass percent as input.

Cancer treatment may be improved by using MSNPs as chemotherapy delivery vessels, which allow for an increased effective drug dose to be delivered to the tumor site due to drug sequestration within the particles during transit to the site, resulting in reduced uptake by the reticuloendothelial system and longer circulation time³⁷. We have provided further insight into this drug delivery system using MSNPs in a murine 4T1 *in vivo* tumor model combined with a mathematical modeling description of drug efficacy. In particular, our mathematical model demonstrates that an increase in MSNPs delivered to the tumor exponentially increases the cell kill at early times in the treatment, leading to improvements in overall treatment outcome. The major hurdle is thus increasing tumor MSNP delivery over current methods, as any increase in delivery to the tumor is expected to significantly improve treatment efficiency. In this perspective, active tumor targeted delivery of chemotherapy via targeting ligand modified nanoparticles^{5,38} is expected to enhance treatment efficacy. We also clarify that, as described in our prior work²³, the drug concentration used to derive the f_{kill} model is the concentration at the blood vessel wall, which is assumed to be a constant and is averaged over the duration of treatment, i.e., the actual drug concentration in the tissue which reaches the tumor was not measured previously. In the present work, we have obtained an actual measurement for the estimated drug concentration in the tissue through measuring the carrier (MSNPs) loaded with Dox in the tumor and MSNP uptake in organs.

Morover, if the quadratic f_{kill} coefficient could be determined early on, the treatment efficacy could be predicted by our mathematical model. It has been demonstrated that tumor exponential growth rate constants were correlated to patient survival³⁹. Here, we demonstrate that, due to external stresses and regression in tumor size due to treatment, the quadratic coefficient following treatment is predictive of treatment uptake and therefore treatment efficacy. Note that θ_f is a combination of parameters, including drug flux across blood vessels, cell death due to accumulated drug, and initial tumor volume (see²³ for details). This implies that θ_f may have a nonlinear relationship with Si content, which has been confirmed in this study where an exponential relation was found. In future efforts, a better understanding of the biodistribution of nanoparticle and Si across organs examined on a larger dataset will allow us to have a more adaptive use of the model presented here. Additionally, further model validation against information obtained from non-invasive imaging modalities such as MRI, PET/CT⁴⁰ will help to quantify nanoparticle-based treatment outcome without the need to sacrifice animals. This important next step will also progress the model towards a more clinical functionality, where it may be implemented as a predictive tool without the need for invasive diagnostic procedures.

Materials and Methods

Mathematical modeling. We recently developed a series of mathematical models in closed form for predicting tumor response to treatment based on time- and space-dependent drug diffusion and perfusion properties^{11,23,32,41–47}. A generalized model presented in²³ can provide predictions of outcome for both conventional chemotherapy with a specific dosing and timing regimen and nanoparticle-based treatment. f_{kill} (i.e., the fraction of tumor killed by treatment) is defined as:

$$f_{\text{kill}} = 1 - \frac{V_i(t)}{V_C(t)}, \quad (1)$$

where V is tumor volume at time t , i indicates drug treatment group (Dox or Dox loaded MSNPs), and C indicates the control group. Normalizing tumor volume at a given time t to initial volume, we have

$$f_{\text{kill}} = 1 - \frac{V_i(t)/V_i(t_0)}{V_C(t)/V_C(t_0)}, \quad (2)$$

where t_0 is determined to be the initial day when treatment was started; in our analysis here, i simply indicates either free DOX or MSNP treatment group.

Assuming that drug-loaded nanoparticles can accumulate within tumors and continuously release drugs at a nearly constant rate over a certain time interval (especially at the initial phase of a treatment), we derived a special form of f_{kill} ²³:

$$f_{\text{kill}} = \frac{F \cdot \lambda_k}{2V_{T,0}} t^2, \quad (3)$$

where F is the flux of drug across blood vessel walls, λ_k is the death rate of tumor cells, $V_{T,0}$ is the tumor volume when tumor begins to respond to treatment (positive f_{kill}), and t is time. Note that there is another key assumption we made to the original f_{kill} model, which is composed of a system of differential equations, in order to develop this simplified form: a drug administered as bolus at a certain dose level has the same effect as the same total amount of drug administered over several months at a constant, smaller dose level. That is, this model functions for a number of situations, including (1) single drug injection at the beginning, (2) multiple drug injections over the course of treatment, and (3) continuous drug administration. Regardless of how we administer the drug, the treatment system can be modeled as a continuous drug delivery system. This assumption has been validated previously *in vivo* and in patients across different types of cancer^{23,32}.

Parameters for best model fits to experimental data (determined by Eq. 2) with the model's predictions from Eq. 3 are derived from:

$$f_{\text{kill}} = \theta_f \cdot t^2, \quad (4)$$

where θ_f is the tumor f_{kill} coefficient $\left(\theta_f = \frac{F \cdot \lambda_k}{2V_{T,0}}\right)$. From our experimental analysis, we obtain:

$$\theta_f = A \cdot e^{B \cdot Si}, \quad (5)$$

where coefficients A and B are fit to determine best values for prediction between Si absolute mass percentage and the model output, θ_f . A and B are tumor and drug specific coefficients specific to 4T1 breast cancer given treatment when tumors are $\sim 500 \text{ mm}^3$ when beginning treatment. A and B are the same for all 5 mice given the treatment described under the experimental description used to describe the relationship between Si mass % deposited in 4T1 breast tumors and θ_f , shown in Fig. 4.

Experiment description. *Accordance statement.* Mouse experiments were performed using protocol approved by the UNM Office of Animal Care Compliance. All methods were carried out in accordance with relevant guidelines and regulations. Six- to eight-week-old female BALB/c female mice were given subcutaneous injections of 5×10^5 4T1 (ATCC® CRL2539™) cells into the right flank. Tumors were grown for two weeks before treatment initiation. Average tumor volumes, calculated from diameters measured externally with calipers, are shown in Fig. 1. Mice were randomly divided into three treatment groups (7 mice/group, 21 mice total): control (PBS), free doxorubicin 1 mg/kg per treatment, 1 mg acetylated MSNPs (50 nm, 2.5 nm pores) loaded with doxorubicin (equivalent 1 mg/kg doxorubicin per treatment). Acetylated MSNPs were made using the protocol described in Townson *et al.*¹², and loaded with doxorubicin using the drug loading protocol for water soluble doxorubicin in Lin *et al.*⁴⁸. Treatment was given starting 2 weeks after tumor cell injections. Treatment days were as follows ($t = 0$ is 2 weeks following tumor injection): 0, 2, 4, and 7. All mice were sacrificed on day 9. Tumor measurements were taken on days: 0, 3, 7, 8, and 9. Tissues were excised and fixed in 4% formaldehyde diluted in PBS, and then Si contents were determined using graphite furnace atomic absorption spectrometry as described below. Statistical analysis was conducted using Matlab, Excel, and Graphpad Prism.

Graphite Furnace Atomic Absorption Spectrophotometry (GFAA). Analysis of Si concentration in MSNP (mesoporous silica nanoparticle) and control (PBS) treated mice tissue was tested using a THGA graphite furnace on a PinAAcle 900 T Atomic Absorption Spectrophotometer (Perkin Elmer, USA). Tissues tested were tumor, kidney, spleen, and liver digested using aqueous tetramethylammonium hydroxide. Absolute mass percentages of silicon in the specific tissue were measured using the standard additions method, commonly used for samples prepared within a matrix that has a strong influence on the analyte signal (the matrix is defined as anything present in the solution that is not the analyte). In the standard additions method, tissues are spiked with differing, known concentrations of Si in order to determine the Si mass % in the tissue measured by extrapolation of the obtained curve of Si signal versus addition to zero addition; a unique signal vs. addition curve is generated for each tissue sample. Tumor (or organ) delivery efficiency, %ID, was determined by using BALB/c standard organ values from Tsai *et al.*⁴⁹ to estimate total organ Si mass deposited. Total Si delivered was calculated based on Si percentage (39.36% of nanoparticle mass) added during synthesis using the protocol in Townson *et al.*¹². Tumor delivery efficiency, %ID, was determined using Si absolute mass percentage in the average control mice each respective organ subtracted from that of the MSNP treated mouse and dividing it by the total administered dose over the treatment duration. The delivery efficiency was measured based on the mass of Si measured in each respective organs divided by the total injected mass of Si (in the form of MSNPs). See Supplementary Information for more details on GFAA methods.

Data availability. All data generated or analyzed during this study are included in this published article and its Supplementary Information files.

References

- Siegel, R. L., Miller, K. D. & Jemal, A. Cancer statistics, 2015. *CA: A Cancer Journal for Clinicians* **65**, 5–29, <https://doi.org/10.3322/caac.21254> (2015).
- Chakrabarti, A., Verbridge, S., Stroock, A., Fischbach, C. & Varner, J. Multiscale Models of Breast Cancer Progression. *Ann Biomed Eng* **40**, 2488–2500, <https://doi.org/10.1007/s10439-012-0655-8> (2012).
- Tang, D. G. Understanding cancer stem cell heterogeneity and plasticity. *Cell Res* **22**, 457–472 (2012).
- Hanessian, S., Grzyb, J. A., Cengelli, F. & Juillerat-Jeanneret, L. Synthesis of chemically functionalized superparamagnetic nanoparticles as delivery vectors for chemotherapeutic drugs. *Bioorganic & Medicinal Chemistry* **16**, 2921–2931, <https://doi.org/10.1016/j.bmc.2007.12.051> (2008).
- Durfee, P. N. *et al.* Mesoporous Silica Nanoparticle-Supported Lipid Bilayers (Protocells) for Active Targeting and Delivery to Individual Leukemia Cells. *ACS Nano* **10**, 8325–8345, <https://doi.org/10.1021/acsnano.6b02819> (2016).
- Shen, H. *et al.* Enhancing Chemotherapy Response with Sustained EphA2 Silencing Using Multistage Vector Delivery. *Clinical Cancer Research* **19**, 1806–1815, <https://doi.org/10.1158/1078-0432.ccr-12-2764> (2013).
- Butler, K. S. *et al.* Protocells: Modular Mesoporous Silica Nanoparticle-Supported Lipid Bilayers for Drug Delivery. *Small* **12**, 2173–2185, <https://doi.org/10.1002/sml.201502119> (2016).
- Wu, X., Wu, M. & Zhao, J. X. Recent development of silica nanoparticles as delivery vectors for cancer imaging and therapy. *Nanomedicine: Nanotechnology, Biology and Medicine* **10**, 297–312, <https://doi.org/10.1016/j.nano.2013.08.008> (2014).
- Krol, S. *et al.* Therapeutic benefits from nanoparticles: the potential significance of nanoscience in diseases with compromise to the blood brain barrier. *Chemical reviews* **113**, 1877–1903, <https://doi.org/10.1021/cr200472g> (2013).
- Li, Z., Barnes, J. C., Bosoy, A., Stoddart, J. F. & Zink, J. I. Mesoporous silica nanoparticles in biomedical applications. *Chemical Society Reviews* **41**, 2590–2605, <https://doi.org/10.1039/C1CS15246G> (2012).
- Pascal, J. *et al.* Mechanistic Modeling Identifies Drug-Uptake History as Predictor of Tumor Drug Resistance and Nano-Carrier-Mediated Response. *ACS Nano* **7**, 11174–11182, <https://doi.org/10.1021/nn4048974> (2013).

12. Townson, J. L. *et al.* Re-examining the Size/Charge Paradigm: Differing *in Vivo* Characteristics of Size- and Charge-Matched Mesoporous Silica Nanoparticles. *Journal of the American Chemical Society* **135**, 16030–16033, <https://doi.org/10.1021/ja4082414> (2013).
13. Han, H. D. *et al.* Enhanced circulation time and antitumor activity of doxorubicin by comblike polymer-incorporated liposomes. *Journal of Controlled Release* **120**, 161–168, <https://doi.org/10.1016/j.jconrel.2007.03.020> (2007).
14. Modo, M. *et al.* Mapping transplanted stem cell migration after a stroke: a serial, *in vivo* magnetic resonance imaging study. *NeuroImage* **21**, 311–317 (2004).
15. Vuu, K. *et al.* Gadolinium-Rhodamine Nanoparticles for Cell Labeling and Tracking via Magnetic Resonance and Optical Imaging. *Bioconjugate Chemistry* **16**, 995–999, <https://doi.org/10.1021/bc050085z> (2005).
16. Chen, F. *et al.* *In Vivo* Tumor Vasculature Targeted PET/NIRF Imaging with TRC105(Fab)-Conjugated, Dual-Labeled Mesoporous Silica Nanoparticles. *Molecular Pharmaceutics* **11**, 4007–4014, <https://doi.org/10.1021/mp500306k> (2014).
17. Shi, S., Chen, F. & Cai, W. Biomedical applications of functionalized hollow mesoporous silica nanoparticles: focusing on molecular imaging. *Nanomedicine* **8**, 2027+ (2013).
18. Huang, H. *et al.* Combination of Lipitor and Celebrex inhibits prostate cancer VCaP cells *in vitro* and *in vivo*. *Anticancer research* **34**, 3357–3363 (2014).
19. Medina-Ramirez, C. M. *et al.* Apoptosis inhibitor ARC promotes breast tumorigenesis, metastasis, and chemoresistance. *Cancer research* **71**, 7705–7715, <https://doi.org/10.1158/0008-5472.can-11-2192> (2011).
20. Cherry, S. R. Multimodality Imaging: Beyond PET/CT and SPECT/CT. *Seminars in nuclear medicine* **39**, 348–353, <https://doi.org/10.1053/j.semnuclmed.2009.03.001> (2009).
21. Chen, F. *et al.* *In Vivo* Tumor Targeting and Image-Guided Drug Delivery with Antibody-Conjugated, Radiolabeled Mesoporous Silica Nanoparticles. *ACS Nano* **7**, 9027–9039, <https://doi.org/10.1021/nn403617j> (2013).
22. Alric, C. *et al.* Gadolinium Chelate Coated Gold Nanoparticles As Contrast Agents for Both X-ray Computed Tomography and Magnetic Resonance Imaging. *Journal of the American Chemical Society* **130**, 5908–5915, <https://doi.org/10.1021/ja078176p> (2008).
23. Wang, Z. H. *et al.* Theory and Experimental Validation of a Spatio-temporal Model of Chemotherapy Transport to Enhance Tumor Cell Kill. *Plos Comput Biol* **12**, <https://doi.org/10.1371/journal.pcbi.1004969> (2016).
24. Arami, H., Khandhar, A., Liggitt, D. & Krishnan, K. M. *In vivo* delivery, pharmacokinetics, biodistribution and toxicity of iron oxide nanoparticles. *Chemical Society Reviews* **44**, 8576–8607, <https://doi.org/10.1039/C5CS00541H> (2015).
25. Miller, J. W., Royalty, J., Henley, J., White, A. & Richardson, L. C. Breast and cervical cancers diagnosed and stage at diagnosis among women served through the National Breast and Cervical Cancer Early Detection Program. *Cancer causes & control: CCC* **26**, 741–747, <https://doi.org/10.1007/s10552-015-0543-2> (2015).
26. Monteiro-Riviere, N. A. & Tran, C. L. *Nanotoxicology: progress toward nanomedicine*. (CRC press, 2014).
27. Noremborg, S. *et al.* Determination of aluminum and silicon in bovine liver by graphite furnace atomic absorption spectrometry after dissolution with tetramethylammonium hydroxide. *Analytical Methods* **7**, 500–506, <https://doi.org/10.1039/C4AY02227K> (2015).
28. Wilhelm, S. *et al.* Analysis of nanoparticle delivery to tumours. *Nature Reviews Materials* **1** (2016).
29. Meng, H. *et al.* Use of Size and a Copolymer Design Feature To Improve the Biodistribution and the Enhanced Permeability and Retention Effect of Doxorubicin-Loaded Mesoporous Silica Nanoparticles in a Murine Xenograft Tumor Model. *ACS Nano* **5**, 4131–4144, <https://doi.org/10.1021/nn200809t> (2011).
30. Chakravarty, R. *et al.* Hollow mesoporous silica nanoparticles for tumor vasculature targeting and PET image-guided drug delivery. *Nanomedicine (London, England)* **10**, 1233–1246 (2015).
31. Benezra, M. *et al.* Multimodal silica nanoparticles are effective cancer-targeted probes in a model of human melanoma. *J Clin Invest* **121**, 2768–2780 (2011).
32. Pascal, J. *et al.* Mechanistic patient-specific predictive correlation of tumor drug response with microenvironment and perfusion measurements. *Proceedings of the National Academy of Sciences* **110**, 14266–14271, <https://doi.org/10.1073/pnas.1300619110> (2013).
33. Bimbo, L. M. *et al.* Inhibition of influenza A virus infection *in vitro* by saliphenylhalamide-loaded porous silicon nanoparticles. *ACS Nano* **7**, 6884–6893, <https://doi.org/10.1021/nn402062f> (2013).
34. Kovalainen, M. *et al.* Development of porous silicon nanocarriers for parenteral peptide delivery. *Mol Pharm* **10**, 353–359, <https://doi.org/10.1021/mp300494p> (2013).
35. McInnes, S. J., Irani, Y., Williams, K. A. & Voelcker, N. H. Controlled drug delivery from composites of nanostructured porous silicon and poly(L-lactide). *Nanomedicine (Lond)* **7**, 995–1016, <https://doi.org/10.2217/nmm.11.176> (2012).
36. Bharti, C., Nagaich, U., Pal, A. K. & Gulati, N. Mesoporous silica nanoparticles in target drug delivery system: A review. *International journal of pharmaceutical investigation* **5**, 124–133, <https://doi.org/10.4103/2230-973X.160844> (2015).
37. Curtis, L. T., Wu, M., Lowengrub, J., Decuzzi, P. & Frieboes, H. B. Computational Modeling of Tumor Response to Drug Release from Vasculature-Bound Nanoparticles. *PLOS ONE* **10**, e0144888, <https://doi.org/10.1371/journal.pone.0144888> (2015).
38. Ashley, C. E. *et al.* The targeted delivery of multicomponent cargos to cancer cells by nanoporous particle-supported lipid bilayers. *Nature materials* **10**, 389–397, <https://doi.org/10.1038/nmat2992> (2011).
39. Stein, W. D. *et al.* Tumor Regression and Growth Rates Determined in Five Intramural NCI Prostate Cancer Trials: The Growth Rate Constant as an Indicator of Therapeutic Efficacy. *Clinical Cancer Research* **17**, 907–917, <https://doi.org/10.1158/1078-0432.ccr-10-1762> (2011).
40. Miccò, M. *et al.* Combined pre-treatment MRI and 18F-FDG PET/CT parameters as prognostic biomarkers in patients with cervical cancer. *European Journal of Radiology* **83**, 1169–1176, <https://doi.org/10.1016/j.ejrad.2014.03.024> (2014).
41. Das, H. *et al.* Impact of Diffusion Barriers to Small Cytotoxic Molecules on the Efficacy of Immunotherapy in Breast Cancer. *PLOS ONE* **8**, e61398, <https://doi.org/10.1371/journal.pone.0061398> (2013).
42. Koay, E. J. *et al.* Transport properties of pancreatic cancer describe gemcitabine delivery and response. *J Clin Invest* **124**, 1525–1536, <https://doi.org/10.1172/JCI73455> (2014).
43. Frieboes, H. B. *et al.* Predictive Modeling of Drug Response in Non-Hodgkin's Lymphoma. *PLOS ONE* **10**, e0129433, <https://doi.org/10.1371/journal.pone.0129433> (2015).
44. Cristini, V., Koay, E. & Wang, Z. *An Introduction to Physical Oncology: How Mechanistic Mathematical Modeling Can Improve Cancer Therapy Outcomes*. (CRC Press, Taylor & Francis Group, 2017).
45. Wang, Z., Butner, J. D., Kerketta, R., Cristini, V. & Deisboeck, T. S. Simulating cancer growth with multiscale agent-based modeling. *Seminars in cancer biology* **30**, 70–78, <https://doi.org/10.1016/j.semcancer.2014.04.001> (2015).
46. Frieboes, H. B. *et al.* Physical oncology: a bench-to-bedside quantitative and predictive approach. *Cancer research* **71**, 298–302, <https://doi.org/10.1158/0008-5472.CAN-10-2676> (2011).
47. Edgerton, M. E. *et al.* A novel, patient-specific mathematical pathology approach for assessment of surgical volume: application to ductal carcinoma *in situ* of the breast. *Anal Cell Pathol (Amst)* **34**, 247–263, <https://doi.org/10.3233/ACP-2011-0019> (2011).
48. Lin, Y.-S., Abadeer, N., Hurley, K. R. & Haynes, C. L. Ultrastable, Redispersible, Small, and Highly Organomodified Mesoporous Silica Nanotherapeutics. *Journal of the American Chemical Society* **133**, 20444–20457, <https://doi.org/10.1021/ja208567v> (2011).
49. Tsai, P. P., Pachowsky, U., Stelzer, H. D. & Hackbarth, H. Impact of environmental enrichment in mice. I: effect of housing conditions on body weight, organ weights and haematology in different strains. *Laboratory animals* **36**, 411–419, <https://doi.org/10.1258/002367702320389071> (2002).

Acknowledgements

This work was supported by the New Mexico Cancer Nanoscience and Microsystems Training Center (CNTC) Graduate Student Fellowship (T.A.B.), the Sandia National Laboratories' Laboratory Directed Research and Development (LDRD) program, and the Lymphoma and Leukemia Society (LLS) (C.J.B.). This work has also been supported in part by the National Science Foundation Grant DMS-1716737 (V.C., Z.W.), the National Institutes of Health (NIH) Grants 1U01CA196403 (V.C., Z.W.), 1U01CA213759 (V.C., Z.W.), 1R01CA226537 (V.C., C.J.B., Z.W.), 1R01CA222007 (V.C., Z.W.), the University of Texas System STARS Award (V.C.), the Rochelle and Max Levit Chair in the Neurosciences (V.C.), and the Methodist Hospital Research Institute (V.C.). Sandia National Laboratories is a multi-mission laboratory managed and operated by National Technology and Engineering Solutions of Sandia, LLC, a wholly owned subsidiary of Honeywell International, Inc., for the U.S. Department of Energy's National Nuclear Security Administration under contract DE-NA0003525.

Author Contributions

T.A.B., C.J.B. and Z.W. conceived and designed the research. T.A.B., E.N.C., P.N.D., Y.-S.L., J.T., E.F.W. and C.J.B. generated and analyzed the experimental data. T.A.B., V.C. and Z.W. performed model analysis. T.A.B., C.J.B. and Z.W. wrote the manuscript, with input from all authors. All authors reviewed and approved the manuscript.

Additional Information

Supplementary information accompanies this paper at <https://doi.org/10.1038/s41598-018-25878-8>.

Competing Interests: The authors declare no competing interests.

Publisher's note: Springer Nature remains neutral with regard to jurisdictional claims in published maps and institutional affiliations.



Open Access This article is licensed under a Creative Commons Attribution 4.0 International License, which permits use, sharing, adaptation, distribution and reproduction in any medium or format, as long as you give appropriate credit to the original author(s) and the source, provide a link to the Creative Commons license, and indicate if changes were made. The images or other third party material in this article are included in the article's Creative Commons license, unless indicated otherwise in a credit line to the material. If material is not included in the article's Creative Commons license and your intended use is not permitted by statutory regulation or exceeds the permitted use, you will need to obtain permission directly from the copyright holder. To view a copy of this license, visit <http://creativecommons.org/licenses/by/4.0/>.

© The Author(s) 2018